



**HAL**  
open science

## Quasi-Vertically Oriented Sb(2)Se(3) Thin-Film Solar Cells with Open-Circuit Voltage Exceeding 500 mV Prepared via Close-Space Sublimation and Selenization

Ping Fan, Guo-Jie Chen, Shuo Chen, Zhuang-Hao Zheng, Muhammad Azam, Nafees Ahmad, Zheng-Hua Su, Guang-Xing Liang, Xianghua Zhang, Zhi-Gang Chen

### ► To cite this version:

Ping Fan, Guo-Jie Chen, Shuo Chen, Zhuang-Hao Zheng, Muhammad Azam, et al.. Quasi-Vertically Oriented Sb(2)Se(3) Thin-Film Solar Cells with Open-Circuit Voltage Exceeding 500 mV Prepared via Close-Space Sublimation and Selenization. ACS Applied Materials & Interfaces, 2021, 13 (39), pp.46671-46680. 10.1021/acsami.1c13223 . hal-03369229

**HAL Id: hal-03369229**

**<https://hal.science/hal-03369229v1>**

Submitted on 15 Jun 2023

**HAL** is a multi-disciplinary open access archive for the deposit and dissemination of scientific research documents, whether they are published or not. The documents may come from teaching and research institutions in France or abroad, or from public or private research centers.

L'archive ouverte pluridisciplinaire **HAL**, est destinée au dépôt et à la diffusion de documents scientifiques de niveau recherche, publiés ou non, émanant des établissements d'enseignement et de recherche français ou étrangers, des laboratoires publics ou privés.

# Quasi-vertically oriented Sb<sub>2</sub>Se<sub>3</sub> thin-film solar cell with open-circuit voltage exceeding 500 mV prepared via close-space sublimation and selenization

Ping Fan<sup>1</sup>, Guo-Jie Chen<sup>1</sup>, Shuo Chen<sup>1</sup>, Zhuang-Hao Zheng<sup>1</sup>, Muhammad Azam<sup>1</sup>, Nafees Ahmad<sup>1</sup>, Zheng-Hua Su<sup>1</sup>, Guang-Xing Liang<sup>\*1</sup>, Xiang-Hua Zhang<sup>2</sup>, Zhi-Gang Chen<sup>3,4</sup>

<sup>1</sup>*Shenzhen Key Laboratory of Advanced Thin Films and Applications, Key Laboratory of Optoelectronic Devices and Systems, College of Physics and Optoelectronic Engineering, Shenzhen University, Shenzhen, 518060, P. R. China*

<sup>2</sup>*Univ Rennes, CNRS, ISCR (Institut des Sciences Chimiques de Rennes) UMR 6226, Rennes, F-35000, France*

<sup>3</sup>*Centre for Future Materials, University of Southern Queensland, Springfield Central, Queensland, 4300, Australia*

<sup>4</sup>*School of Mechanical and Mining Engineering, the University of Queensland, St Lucia, Queensland 4072, Australia*

**Keywords:** Sb<sub>2</sub>Se<sub>3</sub>; solar cell; orientation; open-circuit voltage; close-space sublimation

## **Abstract**

$\text{Sb}_2\text{Se}_3$ , one of the most desirable absorption materials for next-generation thin-film solar cells, has an excellent photovoltaic characteristic. The  $[\text{hk}1]$ -oriented (quasi-vertically oriented)  $\text{Sb}_2\text{Se}_3$  thin film is more beneficial for promoting efficient carrier transport than the  $[\text{hk}0]$ -oriented  $\text{Sb}_2\text{Se}_3$  thin film. Controlling thin-film orientation remains the main obstacle to the further improvement in the efficiency of  $\text{Sb}_2\text{Se}_3$ -based solar cells. In this work, the controlled  $[\text{hk}0]$  or  $[\text{hk}1]$  orientation of the  $\text{Sb}_2\text{Se}_3$  precursor is readily adjusted by tuning the substrate temperature and the distance between the source and the sample in close-space sublimation (CSS). Well-crystallized stoichiometric  $\text{Sb}_2\text{Se}_3$  thin films with the desired orientation and large crystal grains are successfully prepared after selenization.  $\text{Sb}_2\text{Se}_3$  thin-film solar cells in a substrate configuration of glass/Mo/ $\text{Sb}_2\text{Se}_3$ /CdS/ITO/Ag are fabricated with a power conversion efficiency of 4.86% with a record open-circuit voltage ( $V_{\text{OC}}$ ) of 509 mV. The significant improvement in  $V_{\text{OC}}$  is closely related to the quasi-vertically oriented  $\text{Sb}_2\text{Se}_3$  absorber layer with reduced deep-level defect density in the bulk and defect passivation at the  $\text{Sb}_2\text{Se}_3$ /CdS heterojunction. This work indicates that CSS and selenization show a remarkable potential for the fabrication of high-efficiency  $\text{Sb}_2\text{Se}_3$  solar cells.

## **1. Introduction**

Photovoltaic (PV) technology offers a safe, sustainable solution to the worsening global energy crisis by enabling the direct conversion of solar radiation into electricity.<sup>1-3</sup> Thin-film solar cells have the advantage of low cost, high efficiency, and improved device flexibility and are thus viable substitutes to Si-based solar cells. Solar cells based on CdTe and CuInGaSe have achieved the power conversion efficiency (PCE) values of 22.1% and 23.35%, respectively.<sup>4-7</sup> However, their wide practical application is

considerably hindered by the toxicity of Cd and the scarcity of In and Te, which are used in both types of solar cells. Shockley–Queisser theory states that single-junction solar cells with a suitable bandgap ( $E_g \approx 1.14$  eV) of the absorber material can exhibit the maximum PCE of 33.3%.<sup>8</sup>  $\text{Sb}_2\text{Se}_3$  thin-film solar cells have emerged as promising alternatives to other thin-film solar cells and exhibit great potential for low-cost and low-toxicity PV applications because of their attractive optoelectronic properties, such as suitable bandgap (1.1–1.3 eV), high absorption coefficient ( $>10^5$   $\text{cm}^{-1}$  in the visible wavelength region), decent carrier mobility, and stable binary compound composition.<sup>9–</sup>

11

Given that the PCE of  $\text{Sb}_2\text{Se}_3$  thin-film solar cells can increase from 1.9% to 9.2%,  $\text{Sb}_2\text{Se}_3$  is considered to be one of the most desirable photoactive materials for next-generation thin-film solar cells.<sup>9,11–18</sup> However, a few drawbacks, such as open-circuit voltage ( $V_{\text{OC}}$ ) loss and back contact barrier, require urgent solution to further improve the PCE of  $\text{Sb}_2\text{Se}_3$ .<sup>19</sup> The key prerequisite for promoting the PCE of  $\text{Sb}_2\text{Se}_3$  thin-film solar cells is to enhance crystal quality by controlling the orientation of the  $\text{Sb}_2\text{Se}_3$  layer.  $\text{Sb}_2\text{Se}_3$  has a typical one-dimensional (1D) ribbon crystal structure that consists of nanobelts stacked along the x- and c-axes.<sup>20</sup> In the  $[\text{hk}0]$ -orientation, the nanobelts are connected by van der Waals forces, whereas in the  $[\text{hk}1]$ -orientation, the inside of the  $(\text{Sb}_4\text{Se}_6)_n$  ribbons is covalently bonded via Sb–Se bonds along the c-axis.<sup>21–22</sup> In addition, the bonds within the ribbons are stronger than those between the ribbons.<sup>2</sup> The difficult production of ion recombination centers at benign grain boundaries (GBs) implies that electrons are easy to transport in the band but are difficult to conduct between ribbons. Given the 1D structure, GBs parallel to the ribbons can be inherently beneficial for charge–carrier recombination.<sup>23</sup> Previous reports have indicated that  $[\text{hk}1]$ -oriented  $\text{Sb}_2\text{Se}_3$  thin films show improved PCE.<sup>24</sup> Moreover, the PCE of  $\text{Sb}_2\text{Se}_3$

has been found to increase when the [211]-oriented  $\text{Sb}_2\text{Se}_3$  thin films are more dominant than the [221]-orientated  $\text{Sb}_2\text{Se}_3$  thin films.<sup>25</sup> The vapor transport deposition growth process is used to deposit  $\text{Sb}_2\text{Se}_3$  films with preferential [211] and [221] orientations, which show higher PCE values than films with [020] and [120] orientations.<sup>26</sup> Mai's group fabricated high-quality  $\text{Sb}_2\text{Se}_3$  thin films with [221] orientation on the CdS and Mo layers by co-evaporating  $\text{Sb}_2\text{Se}_3$  and Se; the thin films show promising PCE.<sup>27-28</sup> Therefore, controlling the preferred [hk1] orientation in  $\text{Sb}_2\text{Se}_3$  layers is urgently needed to enhance carrier transport and extraction properties to improve PCE.

Generally, devices prepared through physical deposition methods show better device performance in PV applications than those prepared via chemical deposition methods. Close-space sublimation (CSS) is more widely used than other methods for the deposition of a variety of inorganic films, such as the binary compound CdTe, because of its fast processability and high efficiency. These characteristics make CSS a feasible method for industrial-scale manufacturing. Moreover, the film orientation of 1D  $\text{Sb}_2\text{Se}_3$  is sensitive to temperature. According to Fan's early work, CSS is a highly promising method for  $\text{Sb}_2\text{Se}_3$  film deposition because it not only produces large grains with the preferred orientation but is beneficial for controlling grain structure.<sup>17-18,29</sup> Mai's group fabricated high-quality  $\text{Sb}_2\text{Se}_3$  nanorod array solar cells with core-shell structure and efficiency reaching 9.2%.<sup>9</sup> The nanorod arrays along the [hk1]-orientation are highly conducive to light absorption and charge carrier extraction. Despite such advantages, the nanorod arrays have a rough surface that easily leads to electric leakage and large  $V_{\text{OC}}$  deficit<sup>9</sup> likely because the vapor pressure of Se is significantly greater than that of Sb during sublimation; furthermore, the reduction in device performance is attributed to Se vacancies originating from the loss of Se.<sup>30-31</sup> Therefore, we need to explore a new strategy to improve the film quality and device performance of  $\text{Sb}_2\text{Se}_3$  solar cells. Our

group previously reported on the deposition of high-quality  $\text{Sb}_2\text{Se}_3$  thin films with a high  $V_{\text{OC}}$  of 504 mV via a two-step process involving the radiofrequency magnetron sputtering deposition of amorphous  $\text{Sb}_2\text{Se}_3$  followed by post-selenization.<sup>14</sup> In this work, we obtained [hk1]-oriented  $\text{Sb}_2\text{Se}_3$  thin-film solar cells through CSS followed by post-selenization. Notably, the  $V_{\text{OC}}$  of our champion device reached 509 mV, which is higher than that of any other reported  $\text{Sb}_2\text{Se}_3$  thin-film solar cell in the literature.<sup>9,11,14</sup> Our work provides an effective method for manufacturing highly efficient  $\text{Sb}_2\text{Se}_3$  solar cells.

## **2. Experimental detail**

### **2.1. Preparation of $\text{Sb}_2\text{Se}_3$ thin films**

First, soda-lime glass (SLG) substrates were ultrasonically cleaned with detergent, deionized water, isopropanol, ethanol, and deionized water for 20 min. A Mo thin film with a thickness of approximately 1  $\mu\text{m}$  was sputtered on the SLG substrate via magnetron sputtering. The schematic of the preparation process of the  $\text{Sb}_2\text{Se}_3$  thin film is provided in **Fig. 1**. Mai's group fabricated  $\text{Sb}_2\text{Se}_3$  nanorod arrays via CSS,<sup>9</sup> whereas we obtained large  $\text{Sb}_2\text{Se}_3$  grains by performing an additional post-selenization process. The substrate temperature ( $T_{\text{substrate}}$ ) was controlled by using a ceramic light visor inserted between the source and substrate to prevent the overheating of the graphite substrate holder by interactive light radiation. High-purity (>99.99%)  $\text{Sb}_2\text{Se}_3$  powder was compressed in a graphite box. The distance between the source and the sample holder was 9 mm. The pressure of the vacuum chamber was kept below 0.6 Pa prior to deposition. For sublimation, first,  $T_{\text{substrate}}$  and source temperature ( $T_{\text{source}}$ ) were kept at 290 °C for 2 min. Subsequently,  $T_{\text{source}}$  was gradually increased from 290 °C to  $\approx 300$  °C and then to 510 °C for 2 min. The whole sublimation process was completed in 10 min.

The graphite box was naturally cooled down to room temperature when the process was completed. As shown in **Fig. 1**, the as-deposited  $\text{Sb}_2\text{Se}_3$  thin films and 0.2 g of the high-purity Se powder (99.999%) were placed into a double-chamber vacuum tubular furnace. The distance between the Se powder and the sample is 23 cm, and the diameter of the pipe is 50 mm. The chambers were evacuated by using a mechanical pump, and then high-purity argon gas (>99.999%) was introduced to clarify the chambers exhaustively before selenization. A sufficient Se pressure was provided with a high working pressure of  $5 \times 10^4$  Pa to passivate the Se vacancy and obtain a suitable composition. The Se powder side and the  $\text{Sb}_2\text{Se}_3$  thin film side was simultaneously heated to 400 °C and 420 °C for 15 min, respectively. Herein,  $\text{Sb}_2\text{Se}_3$  thin films with different orientations were obtained by exactly controlling  $T_{\text{substrate}}$  and  $T_{\text{source}}$ . The samples deposited at different  $T_{\text{substrate}}$  and  $T_{\text{source}}$  were denoted as S1 ( $T_{\text{substrate}} = 260$  °C and  $T_{\text{source}} = 520$  °C), S2 ( $T_{\text{substrate}} = 260$  °C and  $T_{\text{source}} = 510$  °C), S3 ( $T_{\text{substrate}} = 290$  °C and  $T_{\text{source}} = 510$  °C), and S4 ( $T_{\text{substrate}} = 270$  °C and  $T_{\text{source}} = 520$  °C) and denoted as SS1, SS2, SS3, and SS4, respectively, following post-selenization.

## **2.2. Fabrication of $\text{Sb}_2\text{Se}_3$ thin-film solar cells**

After deposition and selenization, the CdS buffer layer was deposited on the  $\text{Sb}_2\text{Se}_3$  thin films through chemical bath deposition.  $\text{CdSO}_4$  aqueous solution (0.015 M), thiourea aqueous solution (0.75 M), and ammonium hydroxide aqueous solution were subsequently added to the deionized water. The  $\text{Sb}_2\text{Se}_3$  thin films were immersed in the mixed solution and then placed in a water bath at 80 °C under continuous stirring for 9 min. After that, the substrates were rinsed with deionized water and dried in an oven. An ITO window layer was subsequently deposited via magnetron sputtering for 25 min at a power of 110 W and a pressure of 0.4 Pa. Finally, the device surface was scored

into small squares with an identical area of  $0.16 \text{ cm}^2$  by using a knife, and Ag electrodes were deposited as the metallic contact onto the ITO surface by using thermal evaporation.

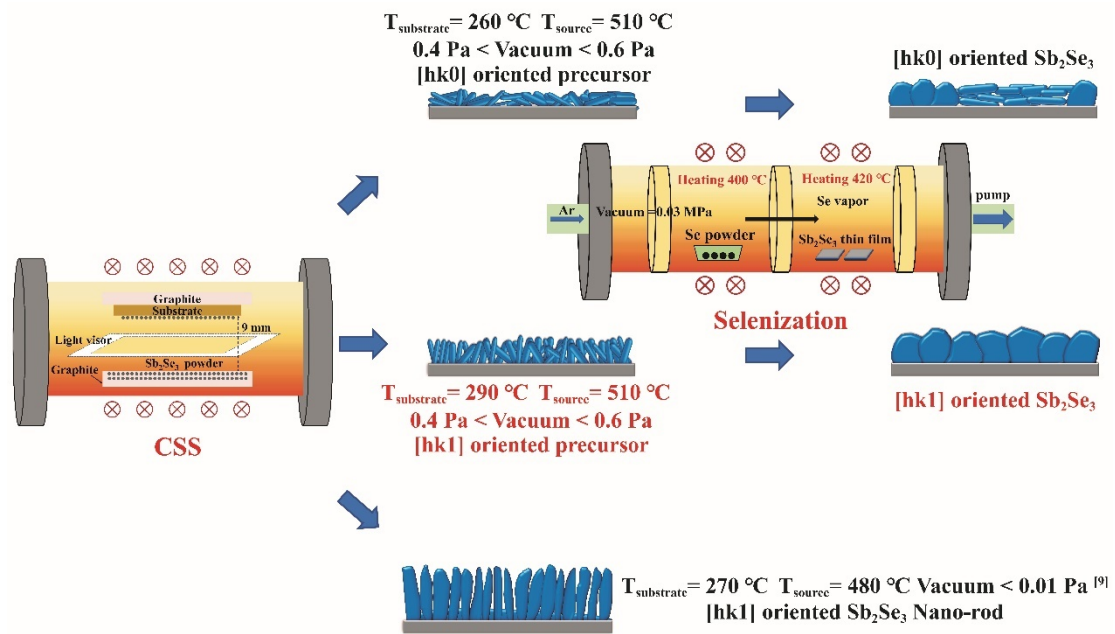


**Fig. 1.** Schematic illustration of the close-spaced sublimated and selenized  $\text{Sb}_2\text{Se}_3$  thin-film.

### 2.3. Characterizations

We analyzed the  $\text{Sb}_2\text{Se}_3$  thin films by using various techniques to determine the effect of temperature on the orientation of film growth and the PCE of the devices. The crystal orientation of the  $\text{Sb}_2\text{Se}_3$  thin films was characterized by applying X-ray diffraction (XRD, Ultima-iv) with  $\text{CuK}\alpha$  radiation under the operation conditions of 40 kV and 40 mA from  $10^\circ$  to  $60^\circ$ . Raman spectra were obtained with an excitation wavelength of 532 nm. The surface and cross-sectional morphologies of the thin films were observed with a thermal field-emission scanning electron microscope (SEM, Zeiss SUPRA 55), and the chemical compositions and elemental distribution of the film were analyzed by using a SEM-coupled energy-dispersive X-ray spectroscope (EDS, BRUKER

QUANTX 200). The current density–voltage (J–V) curves of the Sb<sub>2</sub>Se<sub>3</sub> devices were recorded by using a multimeter (Keithley, 2400 Series) under 100 mW/cm<sup>2</sup> AM 1.5 G light illumination at room temperature. External quantum efficiency (EQE) spectra were acquired by using a Zolix SCS101 system and a Keithley 2400 source meter. Capacitance–voltage (C–V) measurements were obtained at an AC amplitude of 30 mV and a frequency of 10 kHz under dark conditions at room temperature. During C–V measurement, the DC bias voltage was applied from –1 V to 0.3 V. Drive-level capacitance profiling (DLCP) measurements were performed with an AC amplitude from 20 mV to 140 mV and a DC bias voltage from –0.2 V to 0.2 V. Temperature-dependent V<sub>OC</sub> measurements were conducted by using a Lakeshore 325 temperature controller, and the temperatures were swept from 340 K to 160 K in a step of 20 K. Electrochemical impedance spectroscopy (EIS) was conducted by using a CHI600E Electrochemical Workstation. Temperature-dependent capacitance–frequency measurements were performed in the dark with varying temperatures within the range of 210 to 325 K with a 5 K step by using an Agilent 4284A LCR meter. The samples were mounted in a cryostat (Janis Ltd. CCS-150) and cooled with liquid He.

### 3. Results and discussion

XRD measurements were utilized to analyze the crystal orientation and crystallinity of the Sb<sub>2</sub>Se<sub>3</sub> thin films. The XRD patterns are shown in **Fig. 2a** and **2d**. All the diffraction peaks were in good agreement with the information provided by the JCPDS standard card (No. 15–0861) of Sb<sub>2</sub>Se<sub>3</sub> without any detectable impurities. The films showed different preferred orientations at various T<sub>substrate</sub>. Importantly, the [hk0] peak intensities increased when the T<sub>substrate</sub> was less than 270 °C. Previous works have shown that film orientation plays an important role in controlling carrier transport.<sup>11</sup>

The texture coefficient ( $TC$ ) of the diffraction peaks was calculated on the basis of the following equations to investigate the orientations of the  $Sb_2Se_3$  thin films quantitatively:<sup>24</sup>

$$TC(hkl) = \frac{I(hkl)}{I_0(hkl)} / \left( \frac{1}{N} \sum_{i=1}^N \frac{I(h_i k_i l_i)}{I_0(h_i k_i l_i)} \right), \quad (1)$$

where  $I(hkl)$  and  $I_0(hkl)$  are the diffraction peak intensities of the  $[hkl]$  planes in the measured and standard XRD pattern of  $Sb_2Se_3$  (JCPDS 15–0861), respectively. The high  $TC$  of a diffraction peak demonstrates a preferred orientation and an increase in packing density along this designated direction.<sup>24,32</sup> The  $TC$  values of the  $[hk0]$  series of our sample decreased when the  $T_{\text{substrate}}$  was increased from 260 °C to 290 °C during sublimation. By contrast, the  $TC$  value of the  $[hk1]$  and  $[hk2]$  planes stacked vertically on the substrate demonstrated the opposite trend, indicating that a high  $T_{\text{substrate}}$  of 290 °C was suitable for the  $[hk1]$  orientation of the films. The samples were characterized through Raman spectroscopy for the phase analysis of the  $Sb_2Se_3$  absorber layer and further understanding. As shown in **Fig. 2c** and **2f**, all the as-deposited films exhibited three Raman peaks at 189 and 210  $cm^{-1}$ , which were assigned to the Sb–Se vibration in the  $Sb_2Se_3$  pyramidal unit, and a tiny peak at 253  $cm^{-1}$  that could be attributed to the Se–Se bond.<sup>33</sup> The small peaks at 253  $cm^{-1}$  indicated that amorphous Se was present in the as-deposited films.<sup>33-34</sup> After post-selenization treatment, the small peaks disappeared likely because of the transformation of amorphous Se into the crystalline phase.<sup>34</sup> Raman spectroscopy revealed that no impurity phase was present in the  $Sb_2Se_3$  thin film.

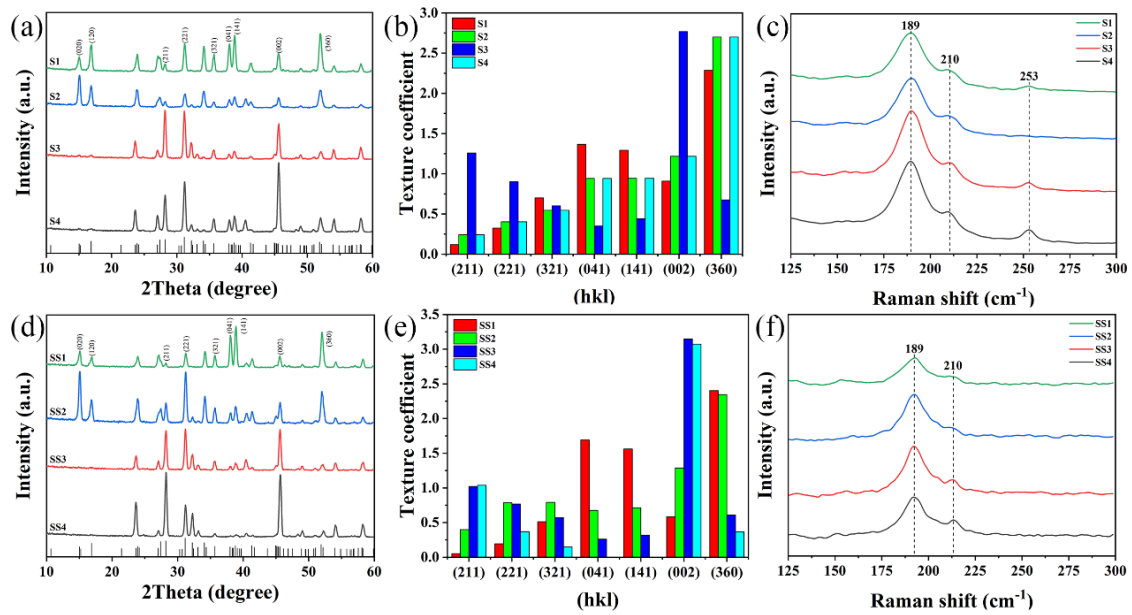


**Fig. 2.** (a) XRD patterns of  $\text{Sb}_2\text{Se}_3$  thin-films with  $T_{\text{substrate}}=260\text{ }^\circ\text{C}$  and  $T_{\text{source}}=520\text{ }^\circ\text{C}$  (S1),  $T_{\text{substrate}}=260\text{ }^\circ\text{C}$  and  $T_{\text{source}}=510\text{ }^\circ\text{C}$  (S2),  $T_{\text{substrate}}=290\text{ }^\circ\text{C}$  and  $T_{\text{source}}=510\text{ }^\circ\text{C}$  (S3),  $T_{\text{substrate}}=270\text{ }^\circ\text{C}$  and  $T_{\text{source}}=510\text{ }^\circ\text{C}$  (S4), respectively. (b) Texture coefficient of  $\text{Sb}_2\text{Se}_3$  thin-films with different temperature (S1, S2, S3 and S4). (c) Raman spectroscopy of different precursor  $\text{Sb}_2\text{Se}_3$  thin-films. XRD patterns (d), Texture coefficients (e) and Raman spectroscopy (f) of the  $\text{Sb}_2\text{Se}_3$  thin-films with a post-selenization treatment, which denoted as SS1, SS2, SS3, and SS4, respectively.

**Fig. 3** and **Fig. 4** present the morphology, cross-sectional SEM images, and water contact angle of the  $\text{Sb}_2\text{Se}_3$  thin films. The morphology of the  $\text{Sb}_2\text{Se}_3$  films was studied via SEM as shown in **Fig. 3a** and **3c**. The surface SEM images of the as-deposited  $\text{Sb}_2\text{Se}_3$  films were similar to those of the nanosheets with  $[\text{hk}0]$  orientation as highlighted by a yellow dotted oval. However, after post-selenization treatment, highly crystallized  $\text{Sb}_2\text{Se}_3$  films with  $[\text{hk}0]$  orientation could be observed on the surface. This observation indicated that post-selenization treatment could increase the degree of crystallinity (**Fig. 3b** and **3d**). Furthermore, the  $[\text{hk}0]$  orientation could be observed in the cross-sectional SEM image of the SS2 device in **Fig. 3f**. In contrast to **Fig. 3**, dense

nanosheets without pinholes could be observed in **Fig. 4**. With the increase in  $T_{\text{substrate}}$ , large crystals could be observed on the surfaces of the nanosheets in **Fig. 4b** and **4d** and grain size reached approximately  $1.5 \mu\text{m}$ , indicating that high  $T_{\text{substrate}}$  during sublimation and the subsequent post-selenization treatment led to large grain sizes with the preferred  $[hk1]$  orientation.<sup>31,35</sup> Large grains are likely more beneficial for carrier transport than  $\text{Sb}_2\text{Se}_3$  nanorod arrays.<sup>9</sup> We assumed that heterojunction quality could be influenced by the chemical interaction between the CdS buffer layer and the  $\text{Sb}_2\text{Se}_3$  absorber layer. We measured the water contact angles of the SS2 and SS3 thin films (**Fig. 3e** and **Fig. 4e**, respectively). The water contact angles of the SS3 and SS2 thin films were  $32.91^\circ$  and  $82.66^\circ$ , respectively. These results indicated that the increased hydrophilic characteristics of SS3 relative to those of SS2 favored CdS infiltration, which may improve  $\text{Sb}_2\text{Se}_3/\text{CdS}$  heterojunction quality.

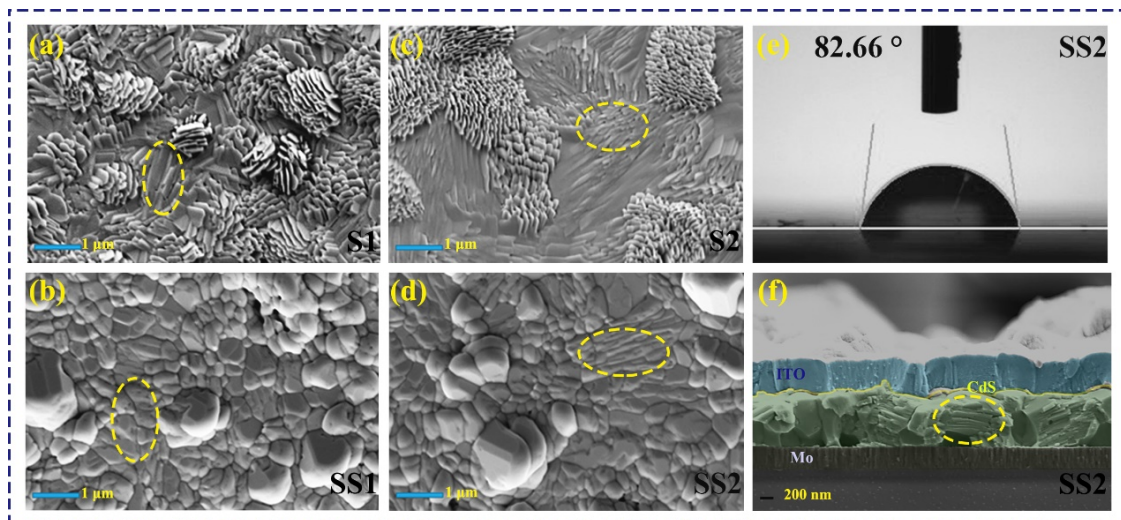


**Fig. 3.** Morphology evolution of  $\text{Sb}_2\text{Se}_3$  thin-film. The morphology of  $\text{Sb}_2\text{Se}_3$  thin-films without and with selenization for S1 (a), SS1 (b), S2 (c), SS2 (d). (e) The water contact angles for the SS2 thin-film. (f) Cross-sectional SEM image for the SS2 thin-film (final device).

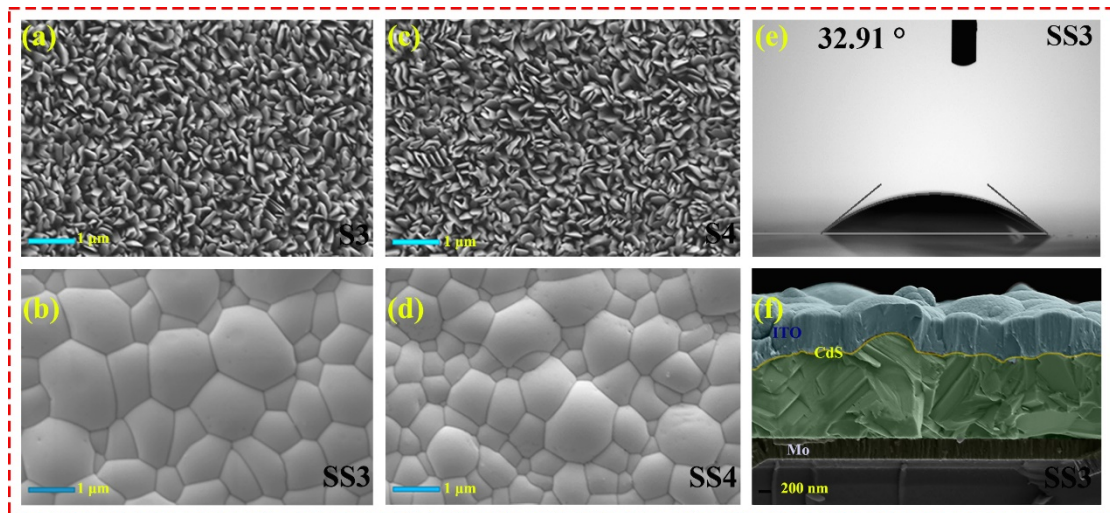


**Fig. 4.** Morphology evolution of  $\text{Sb}_2\text{Se}_3$  thin-film. The morphology of  $\text{Sb}_2\text{Se}_3$  thin-films without and with selenization for S3 (a), SS3 (b), S4 (c), SS4 (d). (e) The water contact angles for the SS3 thin-film. (f) Cross-sectional SEM image for the SS3 thin-film (final device).

An EDS platform equipped with the SEM system was used to characterize the chemical composition of the  $\text{Sb}_2\text{Se}_3$  thin films. The chemical compositions of the as-deposited  $\text{Sb}_2\text{Se}_3$  films and selenized films are shown in **Table 1**. The Se content of all the as-deposited  $\text{Sb}_2\text{Se}_3$  precursor thin films was relatively low. Therefore, through the post-selenization treatment of  $\text{Sb}_2\text{Se}_3$  thin films, the Se vacancy defects in the  $\text{Sb}_2\text{Se}_3$  absorption layer could possibly be reduced during sublimation, thus leading to the recombination suppression of the device. The Se ratios of all the selenized  $\text{Sb}_2\text{Se}_3$  thin films increased. Furthermore, post-selenization treatment could lead to sufficient crystallization, which can reduce interface and bulk defect densities.

**Table 1** The chemical composition of the  $\text{Sb}_2\text{Se}_3$  thin-films deposited at different  $T_{\text{substrate}}$  and  $T_{\text{source}}$  by CSS with and without selenization

Sample	Sb (at. %)	Se (at. %)	Sb/Se ratio
S1	40.67	59.33	0.68
S2	41.27	58.73	0.70
S3	40.36	59.64	0.67
S4	42.33	57.67	0.73
SS1	40.27	59.73	0.67
SS2	38.22	61.78	0.62
SS3	39.16	60.84	0.64
SS4	38.11	61.89	0.62

After fabricating the  $\text{Sb}_2\text{Se}_3$  absorber layer, CdS, ITO, and the front electrode were sequentially fabricated to obtain a device with a substrate configuration of SLG/Mo/ $\text{Sb}_2\text{Se}_3$ /CdS/ITO/Ag. The cross-sectional SEM images of the actual devices (SS2 and SS3) are shown in **Fig. 3f** and **Fig. 4f**. As expected, large  $\text{Sb}_2\text{Se}_3$  grains of the SS3 device penetrated through the whole absorber layer, making it suitable for the transport and extraction of photogenerated carriers. But for the SS2 device, the layered  $\text{Sb}_2\text{Se}_3$  with the [hk0] orientation can be found in **Fig. 3f**. Overall, when the as-deposited  $\text{Sb}_2\text{Se}_3$  precursor films exhibiting nanosheets with [hk1] orientation, high crystallinity with [hk1] preferred orientation could be obtained via the post-selenization process, which is essential for carrier transport to enhance the  $V_{\text{OC}}$ .<sup>31</sup>

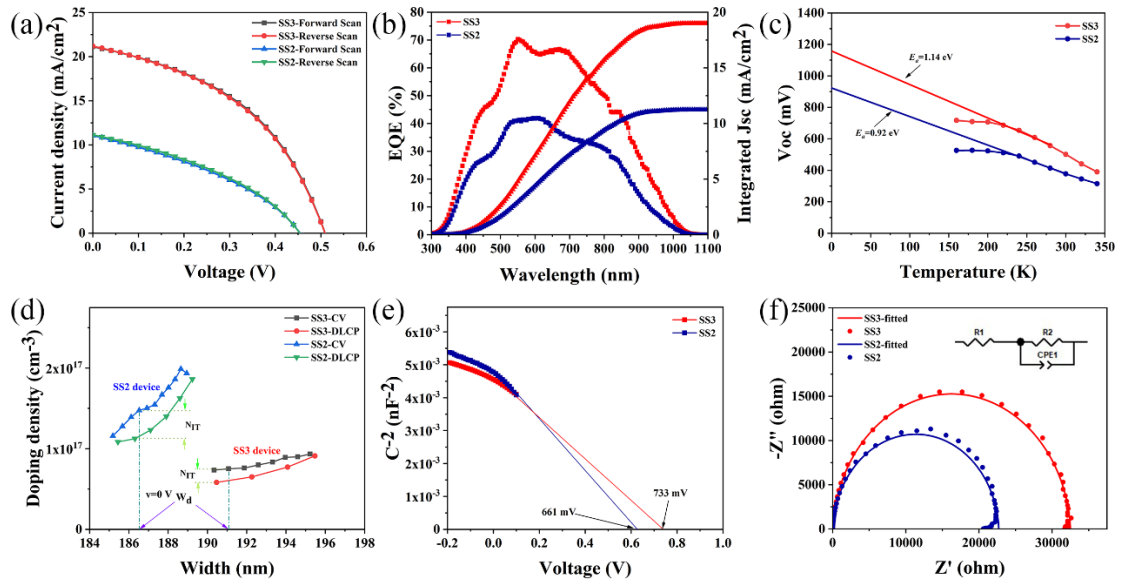


**Fig. 5.** Device performance characterizations of the Sb<sub>2</sub>Se<sub>3</sub> solar cells. (a) The J-V of the SS2 and SS3 devices with different scanning directions. (b) EQE and the integrated J<sub>sc</sub> of SS2 and SS3 devices. (c) Temperature dependent V<sub>oc</sub> measurement, (d) C-V profiling and DLCP measurement, (e) 1/C<sup>2</sup>-V curves and (f) electrochemical impedance spectroscopies of the SS2 and SS3 devices.

The J-V curves of the Sb<sub>2</sub>Se<sub>3</sub> solar cells were obtained under AM 1.5 G light illumination with different scanning directions as shown in **Fig. 5a**. Notably, in both devices, the hysteresis effect was negligible as reflected by the nearly overlapping J-V curves in the forward and reverse scan directions. The detailed PV parameters and the statistical distribution are summarized in **Fig. 6.** and **Table 2.** Most of the SS3 devices presented a high V<sub>oc</sub>, indicating that the stability and reproducibility of this trend is good. The J-V measurement indicated that the SS2 device demonstrated a PCE of 1.94% with a V<sub>oc</sub> of 453 mV, short circuit current density (J<sub>sc</sub>) of 11.47 mA/cm<sup>2</sup>, and fill factor (FF) of 37.32%. By contrast, the SS3 device showed a significant increase in PCE to 4.86% with the corresponding enhancement in V<sub>oc</sub> to 509 mV, J<sub>sc</sub> to 21.15 mA/cm<sup>2</sup>, and FF to 45.10%. This result indicated that increasing the T<sub>substrate</sub> induced

the preferred orientation of the film and further yielded devices with improved efficiencies.<sup>26,36</sup> As shown in **Table 3**, the lower FF value of our device than that of the other devices fabricated via other methods might be ascribed to degradation in the junction and absorber layer quality. The  $V_{OC}$  values of the SS2 and SS3 devices were 453 and 509 mV, respectively, which were higher than those of most high-efficiency  $Sb_2Se_3$  solar cells.<sup>9,11</sup>

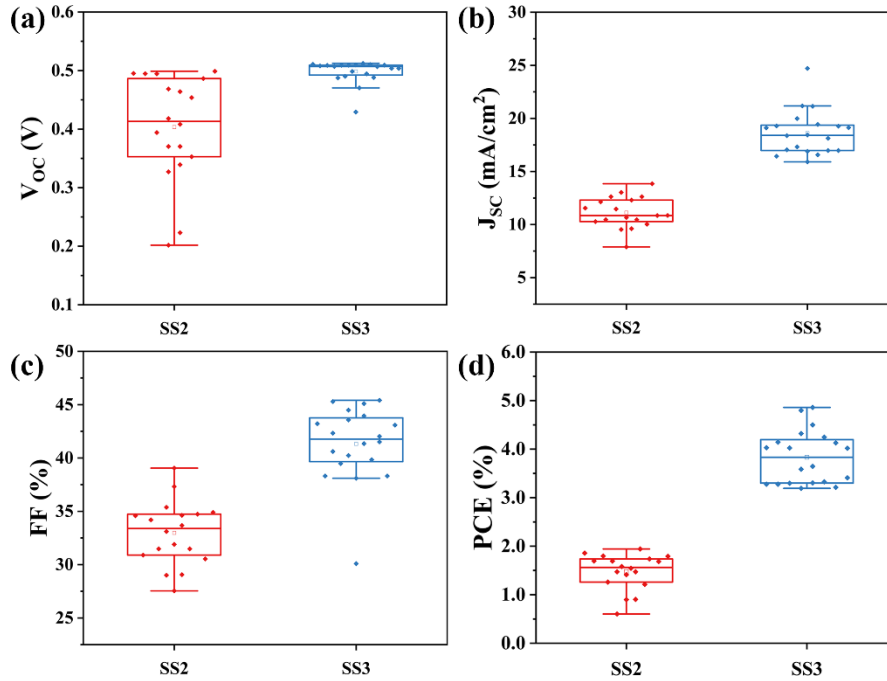


**Fig. 6.** Statistical distribution of the device performance parameters including (a) open-circuit voltage ( $V_{OC}$ ), (b) short-circuit current density ( $J_{SC}$ ), (c) fill factor (FF) and (d) power conversion efficiency (PCE).

**Table 2** Device parameters of the  $Sb_2Se_3$  solar cells fabricated under different temperature

Samples	$V_{OC}$ (mV)	$J_{SC}$ ( $mA/cm^2$ )	FF (%)	Eff (%)
SS3	509	21.15	45.10	4.86
SS2	453	11.47	37.32	1.94

**Table 3** Comparison of device characterize of planer heterojunction  $Sb_2Se_3$  solar cells

via different fabrication methods

Method	Device configuration	V <sub>oc</sub> (mV)	J <sub>sc</sub> (mA/cm <sup>2</sup> )	FF (%)	Eff (%)	Ref.
CSS <sup>a</sup>	Mo/Sb <sub>2</sub> Se <sub>3</sub> /Cd <sub>x</sub> Zn <sub>1-x</sub> S/ZnO/AZO	403	25.69	64.78	6.71	Mai <sup>37</sup>
CSS <sup>a</sup>	SLG/Mo/MoSe <sub>2</sub> /NA-Sb <sub>2</sub> Se <sub>3</sub> /TiO <sub>2</sub> /CdS/ZnO/Al:ZnO	400	32.58	70.3	9.2	Mai <sup>9</sup>
Co-eva <sup>b</sup>	Mo/Sb <sub>2</sub> Se <sub>3</sub> /CdS/ ZnO/AZO/Ag	427	17.11	58.15	4.25	Mai <sup>28</sup>
Sput-Se <sup>c</sup>	Mo/Sb <sub>2</sub> Se <sub>3</sub> /CdS/ ITO/Ag	494	25.91	47.7	6.06	Our work <sup>13</sup>
Sput-Sb-Se <sup>d</sup>	Mo/Sb <sub>2</sub> Se <sub>3</sub> /CdS/ ITO/Ag	504	24.91	54.47	6.84	Our work <sup>14</sup>
CSS-Se <sup>e</sup>	Mo/Sb <sub>2</sub> Se <sub>3</sub> /CdS/ ITO/Ag	509	21.15	45.10	4.86	This work

a Closed space sublimation.

b Co-evaporation.

c Sputtering Sb<sub>2</sub>Se<sub>3</sub> and post-selenization.

d Sputtering Sb precursor and post-selenization.

e Closed space sublimation Sb<sub>2</sub>Se<sub>3</sub> and post-selenization.

The EQE of the SS2 and SS3 devices are presented in **Fig. 5b**. The EQE spectrum of the SS3 device demonstrated a higher photoresponse from 300 nm to 1100 nm than that of the SS2 device. The maximum EQE of the SS3 device was close to 70% at approximately 550 nm, whereas the maximum EQE value of the SS2 device was less than 45% from 300 nm to 1100 nm, indicating that the performance of the SS3 device was considerably better than that of the SS2 device. The reduction in photoresponse was related to undesirable film orientation and thus short electron diffusion length, resulting in lower J<sub>sc</sub>. The electron diffusion length along the [hk1]-oriented grains, which indicated a reduction in dangling bonds and recombination centers at GBs, can reach a high level.<sup>26</sup> However, due to the weak interactions between (Sb<sub>4</sub>Se<sub>6</sub>)<sub>n</sub> ribbons, electrons are difficult to transport in the [hk0]-oriented grains. Further, the EQE values of Sb<sub>2</sub>Se<sub>3</sub> sharply declined from 800 nm to 1100 nm due to the insufficient generation and collection of the carriers leading to a low J<sub>sc</sub>.<sup>31</sup> Moreover, when the [211]

preferentially oriented films were more dominant than the [221] preferentially oriented films, the efficiency of  $\text{Sb}_2\text{Se}_3$  increased.<sup>25</sup> The integrated  $J_{\text{SC}}$  values of the SS2 and SS3 devices calculated from EQE data were 18.98 and 11.22  $\text{mA}/\text{cm}^2$ , respectively, which were in good agreement with the values obtained from J–V measurements.

Temperature-dependent  $V_{\text{OC}}$  measurement was carried out to characterize the carrier transport behavior from 340 K to 140 K and to further analyze interface characteristics.

As shown in **Fig. 5c**, the activation energy ( $E_a$ ) of the dominant recombination within the devices could be calculated by extrapolating the  $V_{\text{OC}}$  curves to the Y-axis.<sup>13</sup> The  $E_a$  of the SS3 device was 1.14 eV, which was very close to the band gap of  $\text{Sb}_2\text{Se}_3$  (1.20 eV), whereas that of the SS2 device was only 0.92 eV. This result implied that interfacial recombination was more prominent for the SS2 device than for the SS3 device mainly due to poor adhesion at the  $\text{Sb}_2\text{Se}_3/\text{CdS}$  interface originating from dangling-bond-rich GBs of the SS2 device.<sup>13</sup>

C–V profiling and DLCP measurements were performed to investigate the interfacial defects of the devices, and the results are shown in **Fig. 5d**. In previous literature,<sup>11</sup> the doping density  $N_{\text{C-V}}$  measured by the C–V includes free carriers, bulk defects, and interfacial defects, whereas the DLCP-measured doping density  $N_{\text{DLCP}}$  only includes free carriers and bulk defects.<sup>13</sup> Hence, the interfacial defects of the device could be calculated via  $N_{\text{C-V}} - N_{\text{DLCP}}$ . The plots of  $N_{\text{C-V}}$  and  $N_{\text{DLCP}}$  against the profiling width  $x$  can be obtained in accordance with the following equations:<sup>38</sup>

$$\left\{ \begin{array}{l} N_{\text{C-V}} = \frac{-2\varepsilon_r n N_D}{\left(\frac{d\left(\frac{1}{C^2}\right)}{dV}\right) q A^2 \varepsilon_0 \varepsilon_r n \varepsilon_r p N_D + 2\varepsilon_r p}, \\ N_{\text{DLCP}} = -\frac{C_0^3}{2q \varepsilon_0 \varepsilon_r p A^2 C_1}, \\ x = \frac{\varepsilon_0 \varepsilon_r p A}{C_0}, \end{array} \right. \quad (2)$$

where  $N_D$  is the doping density of CdS;  $A$  is the device area;  $\epsilon_{r,n}$  and  $\epsilon_{r,p}$  are the relative permittivity of CdS and  $Sb_2Se_3$ , respectively; and  $C_0$  and  $C_1$  are two quadratic fitting parameters derived from the  $C-V$  curves. Considering that DLCP is a purely dynamic measurement and deep defects might affect the depletion width ( $X_d$ ), we used the same x-axis, which represented the distance from the  $Sb_2Se_3/CdS$  interface, for both curves (**Fig. 5d**). The gap between the DLCP and  $C-V$  profiling curves of the SS2 device was large, whereas the discrepancy between both curves of SS3 device was considerably small, implying low defect density and recombination loss at the  $Sb_2Se_3/CdS$  interface. The interface defect densities ( $N_{C-V} - N_{DLCP}$  at zero bias) for the SS2 and SS3 devices were calculated as  $3.504 \times 10^{16}$  and  $1.689 \times 10^{16} \text{ cm}^{-3}$  respectively, indicating that a desirable orientation could enhance the quality of the  $Sb_2Se_3$  absorber. Moreover, the values of  $N_{DLCP}$  for the SS2 device and SS3 device were  $1.13 \times 10^{17}$  and  $5.83 \times 10^{16} \text{ cm}^{-3}$ , respectively. Furthermore, if the carrier concentration was assumed to be constant, then the SS3 device exhibited a lower defect than the SS2 device. This result was supported by the characterization of the morphology of the precursor  $Sb_2Se_3$  thin films (**Fig. 3** and **4**). In addition, the  $X_d$  of the SS3 device was longer than that of the SS2 device, and the interfacial defects originated from dangling-bond-rich GBs would be passivated,<sup>14,17</sup> resulting in reduced defect density and recombination loss. This reduction could account for the higher  $J_{SC}$  of the SS3 device than that of SS2 device. **Fig. 5e** shows the  $1/C^2-V$  curves. The heterojunction-dependent built-in voltage ( $V_{bi}$ ) of the device could be inferred from the X-axis intercept of the  $C-V$  profiling curves. The  $V_{bi}$  value of the SS2 and SS3 devices were 661 and 773 mV, respectively. The difference in  $V_{bi}$  could be attributed to the enhanced built-in-electric field, improved  $Sb_2Se_3/CdS$  interface, and large grain size obtained via the post-selenization process, leading to the remarkable increase in the  $V_{OC}$  of our best device. EIS measurements

were also acquired to analyze the interfacial charge transfer properties of the device. **Fig. 5f** presents the Nyquist plots of the impedance spectra of the different devices, and the equivalent circuit model that was utilized to fit the impedance curves is shown in the inset. The recombination resistance ( $R_s$ ) values of the SS2 and SS3 devices were directly obtained from the arc's diameter length and were 22714 and 32419  $\Omega$ , respectively. Our best device (SS3) exhibited high recombination resistance, which restrained the charge recombination at the  $\text{Sb}_2\text{Se}_3/\text{CdS}$  interface and was responsible for the enhancement in  $V_{OC}$ .

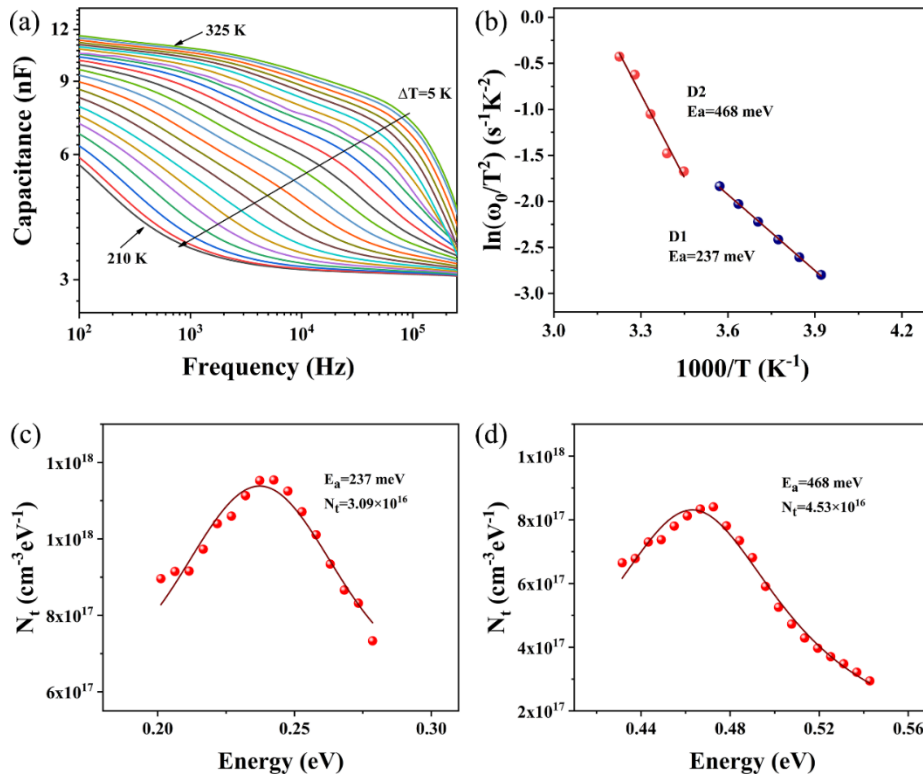


**Fig. 7.** Temperature-dependent admittance results for the champion SS3 device. (a) Capacitance-frequency-temperature (C-f-T) spectra (b) the Arrhenius plots of  $\omega_0/T^2$  versus  $1000/T$  for two defects; the defect activation energies ( $E_a$ ) were calculated for each defect and are shown inside the figure. Defect density of D1 (c) and D2 (d) derived from the admittance spectra.

Admittance spectroscopy measurements, which are usually utilized to speculate the energy level of defects inside the band gap, were acquired to gain a further understanding of the distribution and density of defects in the  $\text{Sb}_2\text{Se}_3$  device.<sup>39</sup> Although admittance spectroscopy involves measuring conductance and capacitance as a function of angular frequency ( $\omega$ ) and temperature (T),

$$Y(\omega, T) = i\omega C(\omega, T) + G(\omega, T), \quad (3)$$

which is the measurement of complex admittance, only capacitance spectra  $C(\omega, T)$  are usually discussed.<sup>40</sup> As illustrated in **Fig. 7a**, the capacitance–frequency (C–f) spectra were obtained over the temperature range of 210 K to 325 K with steps of 5 K and the frequency range of 100 Hz to 1 MHz. Two capacitance steps were obviously distinguishable with different frequencies. These steps could be described as two different defect levels, which were denoted as D1 and D2. The inflection frequencies ( $\omega_0 = 2\pi f_0$ ) corresponding to the admittance spectrum were derived from the angular frequency point  $\omega$  at the maximum of the  $\omega dC/d\omega$  vs.  $\omega$  plot. Defect activation energies ( $E_a$ ) were derived from the slopes of the Arrhenius plots that were linearly fitted based on the following equation:<sup>41-43</sup>

$$\omega_0 = 2\pi\nu_0 T^2 \exp\left(\frac{-E_a}{kT}\right), \quad (4)$$

where  $\nu_0$  is the attempt-to-escape frequency;  $\omega_0$  is the inflection point frequency;  $k$  is the Boltzmann constant; and  $E_a$  is the defect activation energy, representing the average defect energy level relative to the valence band maximum or conduction band minimum. In accordance with the theoretical results obtained through first-principles calculation, the intrinsic defects belonging to  $\text{Sb}_2\text{Se}_3$  could be approximately described as Sb antisite ( $\text{Sb}_{\text{se}}$ ) and Se vacancy ( $\text{V}_{\text{se}}$ ).<sup>30,44</sup> As shown in **Fig. 7b**, D1 could roughly be ascribed to  $\text{V}_{\text{se}}$  vacancy defects with a low  $E_a$  of 237 meV, whereas D2 could roughly be ascribed to  $\text{Sb}_{\text{se}}$  antisite defects with a high  $E_a$  of 468 meV.<sup>45</sup> For the further

evaluation of the defects, the distribution of each defect type was Gaussian-fitted by using the Kimerling model based on the following equations:<sup>46</sup>

$$E(\omega) = kT \ln\left(\frac{2\pi\nu_0 T^2}{\omega}\right), \quad (5)$$

$$N_t(E(\omega)) = -\frac{V_d}{q\omega} \frac{dC}{d\omega} \frac{\omega}{kT}, \quad (6)$$

where  $V_d$  is the built-in potential of the p-n junction,  $\omega$  is the angular frequency, and  $N_t(E[\omega])$  is the defect density. The defect densities of different  $E_a$  are shown in **Fig. 7c** and **d**. The defect densities of the SS3 device were  $3.09 \times 10^{16}$  and  $4.53 \times 10^{16} \text{ cm}^{-3}$ , respectively. These results were almost one order of magnitude higher than the results for a previously reported high-efficiency device likely because the abundance of defects acted as recombination centers, producing recombination losses in the absorber layer and the heterojunction interface that further impaired device performance. In short, with respect to the above discussion, we found that a high-quality absorber layer with the few defects is extremely crucial to the high-performance device.

#### 4. Conclusion

High-quality  $\text{Sb}_2\text{Se}_3$  films were deposited via the CSS method and subjected to post-selenization treatment.  $T_{\text{substrate}}$  significantly influenced the orientation of the precursor films. With the precise control of the  $T_{\text{substrate}}$  and the suitable distance between the source and the sample, the  $\text{Sb}_2\text{Se}_3$  precursor in the preferred quasi-vertical orientation was prepared with the  $T_{\text{substrate}}$  and distance of 290 °C and 9 mm, respectively. After selenization, highly crystallized  $\text{Sb}_2\text{Se}_3$  films in the optimal orientation, which was essential for improving device performance, were obtained. A  $\text{Sb}_2\text{Se}_3$  thin-film solar cell with a PCE of 4.86% was successfully assembled owing to this orientation control

strategy. Notably, our cell demonstrated the record  $V_{OC}$  of 509 mV, which was closely related to deep-level defect suppression in the bulk film and defect passivation at the  $Sb_2Se_3/CdS$  heterojunction. Our effective orientation-controlling strategy via CSS and post-selenization treatment shows a remarkable potential for the further performance improvement of  $Sb_2Se_3$  solar cells.

### **Acknowledgements**

This work was supported by National Natural Science Foundation of China (No. 62074102), Key Project of Department of Education of Guangdong Province (No. 2018KZDXM059), Science and Technology plan project of Shenzhen (JCYJ20190808153409238 and 20200812000347001) and Natural Science Foundation of Guangdong Province (2020A1515010805)

### **References**

- (1) Chen, C.; Bobela, D. C.; Yang, Y.; Lu, S.; Zeng, K.; Ge, C.; Yang, B.; Gao, L.; Zhao, Y.; Beard, M. C.; Tang, J. RRL Physical Properties of  $Sb_2Se_3$  and Its Relevance for Photovoltaics. *Front. Optoelectron* **2017**, *10*, 18-30.
- (2) Mavlonov, A.; Razykov, T.; Raziq, F.; Gan, J.; Chantana, J.; Kawano, Y.; Nishimura, T.; Wei, H.; Zakutayev, A.; Minemoto, T.; Zu, X.; Li, S.; Qiao, L. A Review of  $Sb_2Se_3$  Photovoltaic Absorber Materials and Thin-Film Solar Cells. *Sol. Energy* **2020**, *201*, 227-246.
- (3) Hussain, A.; Arif, S. M.; Aslam, M. Emerging renewable and sustainable energy technologies: State

of the art. *Renew. Sust. Energ. Rev.* **2017**, *71*, 12-28.

(4) Carron, R.; Nishiwaki, S.; Feurer, T.; Hertwig, R.; Avancini, E.; Löckinger, J.; Yang, S. C.; Buecheler, S.; Tiwari, A. N. Advanced Alkali Treatments for High-Efficiency Cu(In,Ga)Se<sub>2</sub> Solar Cells on Flexible Substrates. *Adv. Energy Mater.* **2019**, *9*, No. 1900408.

(5) Green, M. A.; Dunlop, E. D.; Hohl-Ebinger, J.; Yoshita, M.; Kopidakis, N.; Ho-Baillie, A. W. Y. Solar Cell Efficiency Tables (Version 55). *Prog. Photovolt: Res. Appl* **2019**, *28*, 3-15.

(6) Stolterfoht, M.; Le Corre, V. M.; Feuerstein, M.; Caprioglio, P.; Koster, L. J. A.; Neher, D. Voltage-Dependent Photoluminescence and How It Correlates with the Fill Factor and Open-Circuit Voltage in Perovskite Solar Cells. *ACS Energy Lett.* **2019**, *4*, 2887-2892.

(7) Nakamura, M.; Yamaguchi, K.; Kimoto, Y.; Yasaki, Y.; Kato, T.; Sugimoto, H. Cd-Free Cu(In,Ga)(Se,S)<sub>2</sub> Thin-Film Solar Cell with Record Efficiency of 23.35%. *IEEE J.Photovolt.* **2019**, *9*, 1863-1867.

(8) Alharbi, F. H.; Kais, S. Theoretical Limits of Photovoltaics Efficiency and Possible Improvements by Intuitive Approaches Learned From Photosynthesis and Quantum Coherence. *Renew. Sust. Energ. Rev.* **2015**, *43*, 1073-1089.

(9) Li, Z.; Liang, X.; Li, G.; Liu, H.; Zhang, H.; Guo, J.; Chen, J.; Shen, K.; San, X.; Yu, W.; Schropp, R. E. I.; Mai, Y. 9.2%-Efficient Core-Shell Structured Antimony Selenide Nanorod Array Solar Cells. *Nat. Commun.* **2019**, *10*, No. 125.

(10) Wang, L.; Li, D.; Li, K.; Chen, C.; Deng, H.; Gao, L.; Zhao, Y.; Jiang, F.; Li, L.; Huang, F.; He, Y.; Song, H.; Niu, G.; Tang, J. Stable 6%-Efficient Sb<sub>2</sub>Se<sub>3</sub> Solar Cells with a ZnO Buffer Layer. *Nat. Energy* **2017**, *2*, No. 17046.

(11) Wen, X.; Chen, C.; Lu, S.; Li, K.; Kondrotas, R.; Zhao, Y.; Chen, W.; Gao, L.; Wang, C.; Zhang, J.;

Niu, G.; Tang, J. Vapor Transport Deposition of Antimony Selenide Thin Film Solar Cells with 7.6% Efficiency. *Nat. Commun.* **2018**, *9*, No. 2179

(12) Li, Z.; Ni, M.; Feng, X. Simulation of the  $\text{Sb}_2\text{Se}_3$  Solar Cell with a Hole Transport Layer. *Mater. Res. Express.* **2020**, *7*, No. 016416.

(13) Tang, R.; Zheng, Z.; Su, Z.; Li, X.; Wei, Y.; Zhang, X.; Fu, Y.; Luo, J.; Fan, P.; Liang, G. Highly Efficient and Stable Planar Heterojunction Solar Cell Based on Sputtered and Post-selenized  $\text{Sb}_2\text{Se}_3$  Thin Film. *Nano Energy* **2019**, *64*, No. 103929.

(14) Liang, G.; Luo, Y.; Chen, S.; Tang, R.; Zheng, Z.; Li, X.; Liu, X.; Liu, Y.; Li, Y.; Chen, X.; Su, Z.; Zhang, X.; Ma, H.; Fan, P. Sputtered and Selenized  $\text{Sb}_2\text{Se}_3$  Thin-Film Solar Cells with Open-Circuit Voltage Exceeding 500 mV. *Nano Energy* **2020**, *73*, No. 104806.

(15) Tiwari, K. J.; Neuschitzer, M.; Espíndola-Rodríguez, M.; Sánchez, Y.; Jehl, Z.; Vidal-Fuentes, P.; Saucedo, E.; Malar, P. Efficient  $\text{Sb}_2\text{Se}_3/\text{CdS}$  Planar Heterojunction Solar Cells in Substrate Configuration with (hk0) Oriented  $\text{Sb}_2\text{Se}_3$  Thin Films. *Sol. Energy Mater. Sol. Cells* **2020**, *215*, No. 110603

(16) Liang, G.; Chen, X.; Tang, R.; Liu, Y.; Li, Y.; Luo, P.; Su, Z.; Zhang, X.; Fan, P.; Chen, S. Spark Plasma Sintering of  $\text{Sb}_2\text{Se}_3$  Sputtering Target Towards Highly Efficient Thin Film Solar Cells. *Sol. Energy Mater. Sol. Cells* **2020**, *211*, No. 110530.

(17) Guo, L.; Zhang, B.; Ranjit, S.; Wall, J.; Saurav, S.; Hauser, A. J.; Xing, G.; Li, L.; Qian, X.; Yan, F. Interface Engineering via Sputtered Oxygenated  $\text{CdS}:\text{O}$  Window Layer for Highly Efficient  $\text{Sb}_2\text{Se}_3$  Thin-Film Solar Cells with Efficiency Above 7%. *Sol. RRL* **2019**, *3*, No. 1900225.

(18) Guo, L.; Zhang, B.; Qin, Y.; Li, D.; Li, L.; Qian, X.; Yan, F. Tunable Quasi-One-Dimensional Ribbon Enhanced Light Absorption in  $\text{Sb}_2\text{Se}_3$  Thin-film Solar Cells Grown by Close-Space Sublimation. *Sol. RRL* **2018**, *2*, No. 1800128.

- (19) Luo, Y.; Tang, R.; Chen, S.; Hu, J.; Liu, Y.; Li, Y.; Liu, X.; Zheng, Z.; Su, Z.; Ma, X.; Fan, P.; Zhang, X.; Ma, H.; Chen, Z.; Liang, G. An Effective Combination Reaction Involved with Sputtered and Selenized Sb Precursors for Efficient  $\text{Sb}_2\text{Se}_3$  Thin Film Solar Cells. *Chem. Eng. J.* **2020**, *393*, No. 124599.
- (20) Steinmann, V.; Brandt, R.; Buonassisi, T. Photovoltaics: Non-cubic Solar Cell Materials. *Nat. Photonics* **2015**, *9*, 355-357.
- (21) Pattini, F.; Rampino, S.; Mezzadri, F.; Calestani, D.; Spaggiari, G.; Sidoli, M.; Delmonte, D.; Sala, A.; Gilioli, E.; Mazzer, M. Role of the Substrates in the Ribbon Orientation of  $\text{Sb}_2\text{Se}_3$  Films Grown by Low-Temperature Pulsed Electron Deposition. *Sol. Energy Mater Sol. Cells* **2020**, *218*, No. 110724.
- (22) Zeng, K.; Xue, D.; Tang, J. Antimony Selenide Thin-film Solar Cells. *Semicond. Sci. Technol.* **2016**, *31*, No. 063001.
- (23) Caracas, R.; Gonze, X. First-principles Study of the Electronic Properties of  $\text{A}_2\text{B}_3$  Minerals, with  $\text{A}=\text{Bi}, \text{Sb}$  and  $\text{B}=\text{S}, \text{Se}$ . *Phys. Chem. Miner.* **2005**, *32*, 295-300.
- (24) Li, K.; Chen, C.; Lu, S.; Wang, C.; Wang, S.; Lu, Y.; Tang, J. Orientation Engineering in Low-Dimensional Crystal-Structural Materials via Seed Screening. *Adv. Mater.* **2019**, *31*, No. 1903914.
- (25) Guo, L.; Zhang, B.; Li, S.; Zhang, Q.; Buettner, M.; Li, L.; Qian, X.; Yan, F. Scalable and Efficient  $\text{Sb}_2\text{S}_3$  Thin-film Solar Cells Fabricated by Close Space Sublimation. *APL Mater.* **2019**, *7*, No. 041105.
- (26) Zhou, Y.; Wang, L.; Chen, S.; Qin, S.; Liu, X.; Chen, J.; Xue, D.; Luo, M.; Cao, Y.; Cheng, Y.; Sargent, E. H.; Tang, J. Thin-film  $\text{Sb}_2\text{Se}_3$  Photovoltaics with Oriented One-Dimensional Ribbons and Benign Grain Boundaries. *Nat. Photonics* **2015**, *9*, 409-415.
- (27) Li, Z.; Zhu, H.; Guo, Y.; Niu, X.; Chen, X.; Zhang, C.; Zhang, W.; Liang, X.; Zhou, D.; Chen, J.; Mai, Y. Efficiency Enhancement of  $\text{Sb}_2\text{Se}_3$  Thin-film Solar Cells by the Co-evaporation of Se and  $\text{Sb}_2\text{Se}_3$ . *Appl. Phys. Express* **2016**, *9*, No. 052302.

- (28) Li, Z.; Chen, X.; Zhu, H.; Chen, J.; Guo, Y.; Zhang, C.; Zhang, W.; Niu, X.; Mai, Y. Sb<sub>2</sub>Se<sub>3</sub> Thin Film Solar Cells in Substrate Configuration and the Back Contact Selenization. *Sol. Energy Mater Sol. Cells* **2017**, *161*, 190-196.
- (29) Hutter, O. S.; Phillips, L. J.; Durose, K.; Major, J. D. 6.6% Efficient Antimony Selenide Solar Cells Using Grain Structure Control and An Organic Contact Layer. *Sol. Energy Mater Sol. Cells* **2018**, *188*, 177-181.
- (30) Liu, X.; Xiao, X.; Yang, Y.; Xue, D.; Li, D.; Chen, C.; Lu, S.; Gao, L.; He, Y.; Beard, M. C.; Wang, G.; Chen, S.; Tang, J. Enhanced Sb<sub>2</sub>Se<sub>3</sub> Solar Cell Performance Through Theory-guided Defect Control. *Prog. Photovolt: Res. Appl* **2017**, *25*, 861-870.
- (31) Liu, X.; Qiao, Y.; Liu, Y.; Liu, J.; Jia, E.; Chang, S.; Shen, X.; Li, S.; Cheng, K. Enhanced Open Circuit Voltage of Sb<sub>2</sub>Se<sub>3</sub>/CdS Solar Cells by Annealing Se-rich Amorphous Sb<sub>2</sub>Se<sub>3</sub> Films Prepared via Sputtering Process. *Sol. Energy* **2020**, *195*, 697-702.
- (32) Park, S.; Kim, S.; Lee, S.; Sung, S.; Yang, K.; Kang, J.; Kim, D. Controlled Synthesis of (hk1) Preferentially Oriented Sb<sub>2</sub>Se<sub>3</sub> Rod Arrays by Co-evaporation for Photovoltaic Applications. *J. Mater. Chem. A* **2019**, *7*, 25900-25907.
- (33) Vidal-Fuentes, P.; Guc, M.; Alcobe, X.; Jawhari, T.; Placidi, M.; Pérez-Rodríguez, A.; Saucedo, E.; Roca, V. I. Multiwavelength Excitation Raman Scattering Study of Sb<sub>2</sub>Se<sub>3</sub> Compound: Fundamental Vibrational Properties and Secondary Phases Detection. *2D Mater* **2019**, *6*, No. 045054.
- (34) Yannopoulos, S. N.; Andrikopoulos, K. S. Raman Scattering Study on Structural and Dynamical Features of Noncrystalline Selenium. *J. chem. Phys.* **2004**, *121*, 4747-4758.
- (35) Leng, M.; Luo, M.; Chen, C.; Qin, S.; Chen, J.; Zhong, J.; Tang, J. Selenization of Sb<sub>2</sub>Se<sub>3</sub> Absorber Layer: An Efficient Step to Improve Device Performance of CdS/Sb<sub>2</sub>Se<sub>3</sub> Solar Cells. *Appl. Phys. Lett.*

**2014**, *105*, No. 083905.

(36) Guo, H.; Chen, Z.; Wang, X.; Cang, Q.; Jia, X.; Ma, C.; Yuan, N.; Ding, J. Enhancement in the Efficiency of Sb<sub>2</sub>Se<sub>3</sub> Thin-Film Solar Cells by Increasing Carrier Concentration and Inducing Columnar Growth of the Grains. *Sol. RRL* **2019**, *3*, No. 1970033.

(37) Li, G.; Li, Z.; Liang, X.; Guo, C.; Shen, K.; Mai, Y. Improvement in Sb<sub>2</sub>Se<sub>3</sub> Solar Cell Efficiency through Band Alignment Engineering at the Buffer/Absorber Interface. *ACS Appl. Mater. Interfaces* **2019**, *11*, 828-834.

(38) Luo, M.; Leng, M.; Liu, X.; Chen, J.; Chen, C.; Qin, S.; Tang, J. Thermal Evaporation and Characterization of Superstrate CdS/Sb<sub>2</sub>Se<sub>3</sub> Solar Cells. *J. Appl. Phys.* **2014**, *104*, No. 173904.

(39) Li, Y.; Zhou, Y.; Zhu, Y.; Chen, C.; Luo, J.; Ma, J.; Yang, B.; Wang, X.; Xia, Z.; Tang, J. Characterization of Mg and Fe Doped Sb<sub>2</sub>Se<sub>3</sub> Thin Films for Photovoltaic Application. *Appl. Phys. Lett.* **2016**, *109*, No. 232104.

(40) Jasenek, A.; Rau, U.; Nadenau, V.; Schock, H. W. Electronic Properties of CuGaSe<sub>2</sub>-based Heterojunction Solar Cells. Part II. Defect Spectroscopy. *J. Appl. Phys.* **2000**, *87*, 594-602.

(41) Hu, X.; Tao, J.; Weng, G.; Jiang, J.; Chen, S.; Zhu, Z.; Chu, J. Investigation of Electrically-Active Defects in Sb<sub>2</sub>Se<sub>3</sub> Thin-film Solar Cells with up to 5.91% Efficiency via Admittance Spectroscopy. *Sol. Energy Mater Sol. Cells* **2018**, *186*, 324-329.

(42) Eisenbarth, T.; Unold, T.; Caballero, R.; Kaufmann, C. A.; Schock, H.W. Interpretation of Admittance, Capacitance-Voltage, and Current-Voltage Signatures in Cu(In,Ga)Se<sub>2</sub> Thin Film Solar Cells. *J. Appl. Phys.* **2010**, *107*, No. 034509.

(43) Walter, T.; Herberholz, R.; Müller, C.; Schock, H. W. Determination of Defect Distributions from Admittance Measurements and Application to Cu(In,Ga)Se<sub>2</sub> Based Heterojunctions. *J. Appl. Phys.* **1996**,

80, 4411-4420.

(44) Huang, M.; Xu, P.; Han, D.; Tang, J.; Chen, S. Complicated and Unconventional Defect Properties of the Quasi-One-Dimensional Photovoltaic Semiconductor  $\text{Sb}_2\text{Se}_3$ . *ACS Appl. Mater. Interfaces* **2019**, *11*, 15564-15572.

(45) Hu, X.; Tao, J.; Wang, Y.; Xue, J.; Weng, G.; Zhang, C.; Chen, S.; Zhu, Z.; Chu, J. 5.91%-Efficient  $\text{Sb}_2\text{Se}_3$  Solar Cells with a Radio-frequency Magnetron-sputtered CdS Buffer Layer. *Appl. Mater. Today* **2019**, *16*, 367-374.

(46) Li, J.; Kim, S.; Nam, D.; Liu, X.; Kim, J.; Cheong, H.; Liu, W.; Li, H.; Sun, Y.; Zhang, Y. Tailoring the Defects and Carrier Density for Beyond 10% Efficient CZTSe Thin Film Solar Cells. *Sol. Energy Mater. Sol. Cells* **2017**, *159*, 447-455.